Mean-field theories for depinning and their experimental signatures

Cathelijne ter Burg and Kay Jörg Wiese
Laboratoire de Physique de l'Eć ole Normale Supérieure, ENS, Université PSL, CNRS, Sorbonne Université, Université Paris-Diderot, Sorbonne Paris Cité, 24 rue Lhomond, 75005 Paris, France

(Received 3 December 2020; accepted 17 April 2021; published 10 May 2021)

Mean-field theory is an approximation replacing an extended system by a few variables. For depinning of elastic manifolds, these are the position u of its center of mass and the statistics of the forces $F(u)$. There are two proposals how to model the latter: as a random walk (ABBM model), or as uncorrelated forces at integer u (discretized particle model, DPM). While for many experiments the ABBM model (in the literature misleadingly equated with mean-field theory) makes quantitatively correct predictions for the distributions of velocities, or avalanche size and duration, the microscopic disorder force-force correlations cannot grow linearly, and thus unboundedly as a random walk, with distance. Even the effective (renormalized) disorder forces which do so at small distances are bounded at large distances. To describe both regimes, we model forces as an Ornstein-Uhlenbeck process. The latter has the statistics of a random walk at small scales, and is uncorrelated at large scales. By connecting to results in both limits, we solve the model largely analytically, allowing us to describe in all regimes the distributions of velocity, avalanche size, and duration. To establish experimental signatures of this transition, we study the response function, and the correlation function of position u, velocity $\dot{u}$, and forces F under slow driving with velocity $v > 0$. While at $v = 0$ force or position correlations have a cusp at the origin and then decay at least exponentially fast to zero, this cusp is rounded at a finite driving velocity. We give a detailed analytic analysis for this rounding by velocity, which allows us, given experimental data, to extract the timescale of the response function, and to reconstruct the force-force correlator at $v = 0$. The latter is the central object of the field theory, and as such contains detailed information about the universality class in question. We test our predictions by careful numerical simulations extending over up to ten orders in magnitude.

DOI: 10.1103/PhysRevE.103.052114

I. INTRODUCTION

A. Mean-field theories

The framework of disordered elastic manifolds covers such diverse systems as contact-line depinning [1], charge-density waves, magnetic domain walls [2–6], earthquakes [7–16], shear of micropillars [17], and stretching of a knit [18]. Many of these experiments, or at least aspects thereof, are successfully described by *mean-field theory*. But what exactly is meant by *mean-field theory*? Let us define *mean-field theory as a theory which reduces an extended system to a single or a few degrees of freedom*. For depinning these are u, the center of mass of the interface, and the correlations of $F(u)$, the forces acting on it. The center of mass of the interface follows the equation of motion

$$\partial_t u(t) = m^2[w - u(t)] + F(u(t)). \tag{1}$$

The first term is the force exerted by a confining well, equivalent to a Hookean spring with spring constant m^2. The second term $F(u)$ is a random force, possibly the derivative of a random potential, $F(u) = -V'(u)$. Specifying the correlations of $F(u)$ specifies the system, and *selects one mean-field theory*. However, when the reader encounters the term "mean-field theory" in the literature, it is quite generally employed for a model where the forces perform a random walk,

$$\partial_u F(u) = \xi(u), \tag{2}$$

$$\langle \xi(u)\xi(u')\rangle = 2\delta(u - u'). \tag{3}$$

This model was introduced in 1990 by Alessandro, Beatrice, Bertotti, and Montorsi (ABBM) [19,20] to describe magnetic domain walls, and is nowadays referred to as the ABBM model.

The *forces* $F(u)$ are the *coercive magnetic fields* pinning the domain wall, which were observed experimentally to change with a *seemingly* uncorrelated function $\xi(u)$ [21]. The decision of ABBM [19] to model $\xi(u)$ in Eq. (3) as a white noise is a strong assumption, *a posteriori* justified by the applicability to experiments [20]. It means that $F(u)$ has the statistics of a random walk, with force-force correlations

$$\Delta_0^{\mathrm{RW}}(0) - \Delta_0^{\mathrm{RW}}(u - u') := \tfrac{1}{2}\overline{[F(u) - F(u')]^2} = |u - u'|. \tag{4}$$

Actually, Eqs. (2)–(3) are the final model analyzed by ABBM. What they considered first are forces modeled as an Ornstein-Uhlenbeck process,

$$\partial_u F(u) = -F(u) + \xi(u). \tag{5}$$

Note that by rescaling m^2 and time t in Eq. (1), noise strength "2" in Eq. (3) and the amplitude "1" for the restoring force in Eq. (5) can always be achieved. Thus the only parameter of relevance is m^2. With the noise in Eq. (3), the process (5) has correlations (see Appendix A),

$$\Delta_0^{\mathrm{OU}}(u - u') := \overline{F(u)F(u')}^{\mathrm{c}} = e^{-|u-u'|}, \tag{6}$$

i.e., it is uncorrelated at large distances. One explicitly checks that the small-distance behavior of $\Delta_0^{\mathrm{OU}}(u - u')$ is as in

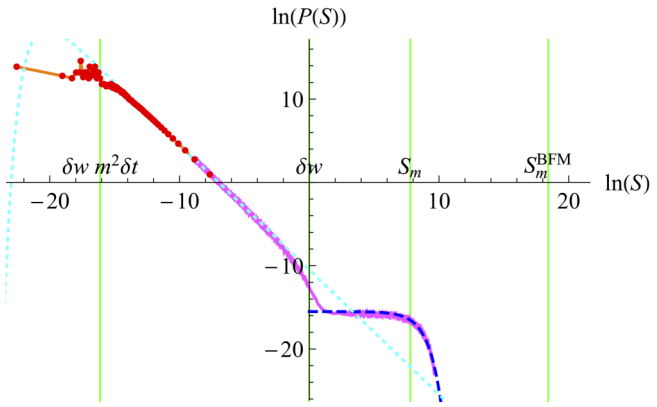

FIG. 1. Avalanche-size distribution $P(S)$ for a particle with forces given by Eq. (5). The theoretical curves are the kicked ABBM model as given by Eq. (46) (cyan dotted), and the DPM as given by Eq. (62) (blue dashed). Improved numerical solver (INS), $m^2 = 10^{-4}$, $\delta w = 1$, $\delta t = 10^{-4}$, $S_m := \langle S^2\rangle/(2\langle S\rangle) = 2408.89$, $\rho_m = 2329.95$, $N = 10^8$.

Eq. (4). This is the model we study in this article. Contrary to the claim made by ABBM in Ref. [19] (beginning of Sec III), even at low domain-wall velocities the reduced model (2) is only valid at small scales, and there is always an observable, namely the renormalized disorder correlator defined below in Eq. (17), which quantifies whether forces are distributed according to an Ornstein-Uhlenbeck process or a random walk.

An example for the differences between the two models is given in Fig. 1, which shows the avalanche-size distribution, assuming forces generated by the Ornstein-Uhlenbeck process (5). One sees that, for small avalanche sizes S, the probability distribution follows $P(S)$ as predicted for the ABBM model, with no adjustable scale, and a critical exponent $\tau_{\rm ABBM} = 3/2$ (defined in Table I). However, when the avalanche size reaches the correlation length of the forces, which according to Eq. (6) is $\xi_F = 1$ in our units, the avalanche-size distribution crosses over to a pure exponential, formally equivalent to an avalanche-size exponent $\tau_{\rm DPM} = 0$. As can be seen in Fig. 1 and is summarized in Table I, it also drastically changes the scaling of the large-scale cutoff, from $S_m^{\rm ABBM} \equiv S_m^{\rm BFM} \sim m^{-4}$, to $S_m^{\rm DPM} \sim m^{-2}$.

Up to now, we have only discussed mean-field models. Field theory [22–24] gives a more differentiated view: First of all, mean-field theory should be applicable for $d = d_{\rm c}$ [25,26], a case which contains magnets with strong dipolar interactions [5], earthquakes [9], and micropillar shear experiments [17]. As $F(u)$ has the statistics of a random walk, the (microscopic) force-force correlator of Eqs. (2)–(3), as given in Eq. (4), grows linearly with distance. A linearly increasing correlation function is at the microscopic level predicted for the correlations of the potential, $R(0) - R(u) := \frac{1}{2}\langle[V(u)-V(0)]^2\rangle$, if the disorder is of the random-field type, the strongest microscopic disorder at our disposal [27,28]. We know of no microscopic mechanism to generate the correlations of Eq. (4). On the other hand, the effective (renormalized) force-force correlator $\Delta(u)$ has a cusp [28–30], so Eq. (4) with $|\Delta'(0^+)| = 1$ is an approximation, valid for small u. The ABBM model defined by Eqs. (1)–(3) should then be viewed as an effective theory, arriving *after renormalization*, and valid for small u only.

If indeed the microscopic disorder has the statistics of a random walk, then the force-force correlator (4) does not change under renormalization, as is easily checked by inserting it into the one-loop or two-loop flow equations for depinning [23,24]. Counting of derivatives for higher-order corrections proves that this statement persists to all orders in perturbation theory. Even an extended (non-mean-field) system where each degree of freedom sees a force which has the statistics of a random walk, is stable under renormalization. An example is the Brownian-force model (BFM) introduced in Ref. [31], which has a roughness exponent $\zeta_{\rm BFM} = 4 - d$,

TABLE I. Comparison of the ABBM model with the DPM.

ABBM model	Discretized particle model (DPM)
Characteristic scale of effective (renormalized) force correlator	
1	$\rho_m = (m^2\sqrt{2\ln(m^{-2})})^{-1}$
Effective (renormalized) disorder $\Delta(w)$	
$\Delta(0) - \Delta(w) = \sigma\lvert w\rvert$, $\sigma = 1$	$\Delta(w) = m^4\rho_m^2\left[\mathrm{Li}_2(1 - e^{\lvert w\rvert/\rho_m}) + \frac{w^2}{2\rho_m^2} + \frac{\pi^2}{6}\right]$
Critical force	
$f_{\rm c}(m^2) = F(u=0)$	$f_{\rm c}(m^2) = \sqrt{2\ln(m^{-2})}$
Response function $R(t) = \tau^{-1}e^{-t/\tau}$	
$\tau^{-1} = m^2$	$\tau^{-1} = \tau_m^{-1} := 2m^2\ln(m^{-2})$
Avalanche-size distribution for infinitesimal kick $P(S) \sim S^{-\tau}e^{-S/S_m}$	
$\tau = 3/2$, $S_m = m^{-4}$	$\tau = 0$, $S_m = \rho_m$
Avalanche-duration distribution for infinitesimal kick $P(T) \sim T^{-\alpha}e^{-T/T_m}$	
$\alpha = 2$, $T_m = \tau = m^{-2}$	$\alpha = 0$, $T_m = \tau_m = [2m^2\ln(m^{-2})]^{-1}$
Roughness exponent ζ, defined by $u \sim m^{-\zeta}$	
$\zeta = 4$	$\zeta = 2^-$ (2 reduced by logarithmic corrections)

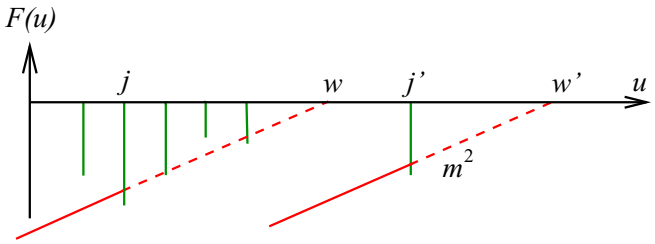

FIG. 2. Geometric solution to find u_w as a function of w for the DPM model of [33].

where d is the dimension of the elastic object. This was indirectly verified numerically in Ref. [32].

Our discussion below shows that the ABBM model (2)–(3) is adequate only at small distances, but fails at larger ones, where the force-force correlator decorrelates. We therefore expect that at large distances it crosses over to a model of uncorrelated random forces. Such a model, which we term the *discretized particle model* (DPM), was introduced in Ref. [33]. In this model, the random forces are modeled by needles at integer positions, blocking the advance of the particle. Figure 2 shows this model, and how to geometrically construct the solution of Eq. (1): Draw a straight line $f(u) := m^2(u - w)$ of slope m^2, intersecting the horizontal axis ($F = 0$) at $u = w$. As long as $f(u) < F(u)$, the particle advances. The motion is stopped at the first obstacle this line encounters. In Fig. 2, this is $u(w) = j$ and $u(w') = j'$. It remains to specify the correlations of the random forces $F(j)$, $j \in \mathbb{N}$. As field theory in general supposes Gaussian disorder, we choose $F(j)$ to be Gaussian distributed, with variance

$$\overline{F(j)F(j')} = \delta_{j,j'}. \tag{7}$$

In this article, we wish to study the crossover from ABBM disorder, given by Eqs. (2)–(4), to the correlations (7). We do this by analyzing the Ornstein-Uhlenbeck process (5).

To compare Ornstein-Uhlenbeck forces with the DPM, let us consider their microscopic disorder force-force correlator. For the DPM, with forces constant between integers,[1] it reads

$$\Delta_0^{\mathrm{DPM}}(u - u') = \overline{F(u)F(u')}^{\mathrm{c}} = \max(1 - |u - u'|, 0). \tag{8}$$

Both models have a linear (microscopic) cusp, with

$$-\Delta_0'(0^+) = 1. \tag{9}$$

On the other hand, the integrals over their force-force correlations are different,

$$\int_{-\infty}^{\infty} du\, \Delta_0^{\mathrm{DPM}}(u) = 1, \tag{10}$$

$$\int_{-\infty}^{\infty} du\, \Delta_0^{\mathrm{OU}}(u) = 2. \tag{11}$$

Our working hypothesis to be checked below is that the two models have the same universal large-scale properties, with the same scale, and without any additional parameter. Nevertheless, we expect that nonuniversal quantities such as the critical force might be shifted.

Equation (5) also serves as an effective theory for the crossover, observed in systems of linear size L, from a regime with $mL \gg 1$ described by an extended elastic manifold to a single-particle regime described by the DPM. This crossover has indeed be seen in numerical simulations for a line with periodic disorder [34].

B. The effective disorder and measurements

1. Force correlator at finite driving velocity

The question we are now turning to is the following: What can experiments teach us about the underlying field theory? Can the crossover be seen in an experiment?

Suppose the system is driven quasistatically, i.e.,

$$w = vt, \tag{12}$$

and we wish to study the limit of $v \to 0$. To do so, parametrize the solution of Eq. (1) as

$$u_w := u(t). \tag{13}$$

In this limit most of the time $\partial_t u(x, t) = 0$, and Eq. (1) yields

$$F(u_w) = -m^2(w - u_w). \tag{14}$$

The geometric construction to find this solution is shown in Fig. 2. The critical force is defined as

$$f_{\mathrm{c}}(m) := -\overline{F(u_w)} \equiv m^2\overline{[w - u_w]}. \tag{15}$$

The signs are such that applying the external force f_{c} (counted positive in the driving direction) overcomes the pinning forces $F(u_w)$.

At a finite driving velocity v, averaging Eq. (1) yields an additional term $\bar{u} = v$, leading, at least for small velocity v, to

$$f_{\mathrm{c}}(m) := -\overline{F(u_w)} \equiv m^2\overline{[w - u_w]} - v. \tag{16}$$

The effective disorder force-force correlator is defined as

$$\begin{aligned}\Delta(w - w') &:= \lim_{v\to 0} \overline{F(u_w)F(u_{w'})}^{\mathrm{c}} \\ &= \lim_{v\to 0} m^4\overline{[w - u_w][w' - u_{w'}]}^{\mathrm{c}}.\end{aligned} \tag{17}$$

Note that if we consider an extended system, and u_w is the center of mass position $u_w := \frac{1}{L^d}\int_x u_w(x)$, then there is an additional factor of L^d on the right-hand side (r.h.s.) [29,35].

In a real experiment, it is impossible to measure adiabatically, and instead one measures at a finite velocity,

$$\Delta_v(w - w') := m^4\overline{[w - u_w][w' - u_{w'}]}^{\mathrm{c}}. \tag{18}$$

By definition,

$$\Delta(w - w') = \lim_{v\to 0} \Delta_v(w - w'). \tag{19}$$

While $\Delta(w - w')$ is the second cumulant of the effective action of the field theory [35], the expectation (18) is an observable. Perturbation theory allows us to calculate it as

$$\Delta_v(w) = \int_0^{\infty} dt \int_0^{\infty} dt'\, \Delta(w - vt + vt')R(t)R(t'), \tag{20}$$

[1] To render $\overline{F(u)F(u')}$ function of $u - u'$ only, the needle forces $F(j)$, $j \in \mathbb{N}$ of Fig. 2 are extended to $F(u) = F(j)$, $j \leqslant u < j + 1$. The solutions u_w of Fig. 2 change, $u_w \to u_w - \delta$, with $0 \leqslant \delta < 1$, negligible for small m^2.

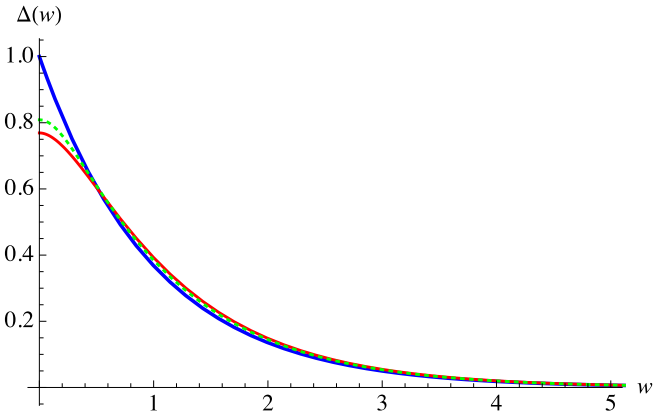

FIG. 3. $\Delta(w) = e^{-w}$ (blue solid), and the finite-velocity correlator (25) (red) for $\tau v = 0.3$, compared to the boundary-layer approximation (27) (green dotted).

where $R(t)$ is the response of the center of mass to an increase in w, and $\int_t R(t) = 1$. (Usually, the response is defined with respect to an increase δF in force. Using $\delta F = m^2 \delta w$, the response with respect to a force is normalized as $\int_t R(t) = 1/m^2$.)

Equation (18) implies that the integral of $\Delta_v(w)$ is independent of v. In general, both $\Delta(w)$ and $R(t)$ may themselves depend on v. We show below in Sec. III H that using the zero-velocity functions on the r.h.s. of Eq. (20) is sufficient at small driving velocities v, and the error made is probably $\mathcal{O}(v^3)$ or smaller; see Fig. 19.

An analytic expression for the amplitude of the rounding can be given by expanding Eq. (20) at $w = 0$ for small v,

$$\begin{aligned}\Delta_v(0) &= \int_0^\infty dt \int_0^\infty dt' \,[\Delta(0) + v\Delta'(0^+)|t - t'| \\ &\quad + \mathcal{O}(v^2)]R(t)R(t') \\ &= \Delta(0) + v\tilde{\tau}\Delta'(0^+) + \mathcal{O}(v^2), \end{aligned} \tag{21}$$

$$\tilde{\tau} := \int_0^\infty dt \int_0^\infty dt' \,|t - t'|R(t)R(t'), \tag{22}$$

$$\tau := \langle t \rangle \equiv \int_0^\infty dt\, R(t)t. \tag{23}$$

If $R(t)$ decays exponentially, then $\tilde{\tau} = \tau$, which should remain a good approximation in most cases.

As an illustration for the operation defined in Eq. (20), consider $\Delta(w) = \Delta(0)e^{-|w|/\xi}$, and

$$R(t) = \tau^{-1} e^{-t/\tau}. \tag{24}$$

Then, as plotted in Fig. 3,

$$\Delta_v(w) = \Delta(0)\, \frac{e^{-|w|/\xi} - \frac{\tau v}{\xi} e^{-|w|/(\tau v)}}{1 - \left(\frac{\tau v}{\xi}\right)^2}. \tag{25}$$

This is a superposition of two exponentials, with the natural scales ξ and τv. Since

$$\Delta_v'(0^+) = 0, \tag{26}$$

the cusp characteristic for depinning at the origin is rounded. This can be proven in general from Eq. (20). Note that $\Delta_v(w)$ is *not* analytic, as the expansion contains a term of order $|w|^3$.

Since experiments are performed at a finite driving velocity, but we are mostly interested in the zero-velocity limit, the question arises of whether the folding of Eq. (20) can be undone. There are several possibilities to do this.

2. Boundary-layer analysis

As long as $\tau v \ll \xi$, the second term of Eq. (25) decays much faster than the first, allowing us to perform a *boundary-layer analysis*. This term was coined in the context of turbulence, where a turbulent bulk behavior has to be connected to a laminar boundary layer. There is a large amount of mathematics and physics literature on the subject. Relevant keywords are *boundary layer* (physics literature) or *singular perturbation theory* (mathematics literature); a few references to start with are [36–39]. Let us proceed by noting that Eq. (20) can be approximated by the boundary-layer ansatz

$$\Delta_v(w) \simeq \mathcal{A}_v\, \Delta\big(\sqrt{w^2 + \delta_w^2}\big), \tag{27}$$

$$\delta_w = \tau v, \quad \tau := \langle t \rangle = \int_0^\infty dt\, R(t)t, \tag{28}$$

$$\mathcal{A}_v = \frac{\int_0^\infty dw\, \Delta(w)}{\int_0^\infty dw\, \Delta\big(\sqrt{w^2 + \delta_w^2}\big)}. \tag{29}$$

The amplitude $\mathcal{A}_v$ ensures normalization. The quality of this approximation can be seen in Fig. 3: it works well for v small, but deteriorates for larger v.

We can use the boundary-layer formula (27) to plot the measured $\Delta_v(w)$ against $\tilde{w} := \sqrt{w^2 + \delta_w^2}$, and then find the best δ_w which removes the curvature of $\Delta_v(w)$. It yields δ_w, and by extrapolation to $w = 0$ the full $\Delta(w)$. This idea is tested below in Sec. III I.

3. Estimate of timescale

If in an experiment the response function is unavailable, using the boundary-layer ansatz (27), its characteristic timescale τ can be reconstructed approximatively from $\Delta_v(w)$ as

$$\delta_w = \tau v \simeq \frac{\lim_{w\to 0} \Delta'(w)}{\Delta_v''(0)}. \tag{30}$$

In the numerator is written $\lim_{w\to 0} \Delta'(w)$, which is obtained by extrapolating $\Delta_v'(w)$ from outside the boundary layer, i.e., $w \geqslant \delta_w = \tau v$, to $w = 0$.

4. Differential equation

First note that the response function $R(t)$ defined in Eq. (24) satisfies the differential equation

$$(\tau \partial_t + 1)R(t) = \delta(t). \tag{31}$$

Second, rewrite Eq. (20) as

$$\begin{aligned}&\Delta_v(v(t - t')) \\ &= \int_{-\infty}^{t} dt_1 \int_{-\infty}^{t'} dt_2\, \Delta(v(t_1 - t_2))R(t - t_1)R(t - t_2). \end{aligned} \tag{32}$$

Applying the differential operator of Eq. (31) both to t and t' yields

$$(\tau\partial_t + 1)(\tau\partial_{t'} + 1)\Delta_v(v(t-t')) = \Delta(v(t-t')). \tag{33}$$

In terms of the variable w, this relation can be simplified to

$$\Delta(w) = \left[1 - (\tau v)^2\partial_w^2\right]\Delta_v(w). \tag{34}$$

While Eq. (34) is more precise, and reconstructs $\Delta_{v=0}(w)$ down to $w = 0$, the boundary-layer analysis may be more robust for noisy data. We will examine these procedures in Sec. III I.

5. *Other autocorrelation functions*

Equation (1) allows us to consider three different observables,

$$u_w = u(t), \tag{35}$$

$$\dot{u}_w = \dot{u}(t), \tag{36}$$

$$F_w = F(u_w) = F(u(t)). \tag{37}$$

What is measured in magnetic domain-wall experiments is the induced current, proportional to $\dot{u}_w$ [2–5]; in contact-line depinning where the interface is filmed, this is u_w [1]; when stretching an elastic material as a knit, this is the *external* force exerted on the knit, itself proportional to $u_w - w$ [18]. We do not know of any system where one can measure solely the force F_w of the disorder.

Equations (35)–(37) define three autocorrelation functions:

$$\Delta_v(w-w') := m^4\overline{[u_w - w][u_{w'} - w')]}^{\rm c}, \tag{38}$$

$$\Delta_{\dot{u}}(w-w') := \overline{[\dot{u}_w - v][\dot{u}_{w'} - v]}^{\rm c}, \tag{39}$$

$$\Delta_F(w-w') := \overline{F_w F_{w'}}^{\rm c}. \tag{40}$$

We will show in Sec. III F that they satisfy

$$\Delta_F(w) = \Delta_v(w) + \Delta_{\dot{u}}(w), \tag{41}$$

$$\Delta_{\dot{u}}(w) = -\frac{v^2}{m^4}\partial_w^2\Delta_v(w). \tag{42}$$

II. REVIEW OF KNOWN RESULTS FOR ABBM AND DPM

Key features for the ABBM model and the DPM are given in Table I.

A. ABBM model

The response function is unchanged from the free theory:

$$R(t) = m^2 e^{-m^2 t}\Theta(t). \tag{43}$$

The velocity distribution $P_t(\dot{u})$ reads [19,40–42]

$$P_t(\dot{u}) = m^2(m^2\dot{u})^{vm^2-1}\frac{e^{-m^2\dot{u}}}{\Gamma(vm^2)}. \tag{44}$$

By construction it is normalized, its first moment is $\langle\dot{u}\rangle = v$, and

$$v_m^{\rm ABBM} := \frac{\langle\dot{u}^2\rangle}{\langle\dot{u}\rangle} = m^{-2} + v. \tag{45}$$

The avalanche-size distribution $P_{\delta w}^S(S)$, given a kick δw, reads [42]

$$P_{\delta w}^S(S) = m^2\delta w\frac{e^{-\frac{m^4(S-\delta w)^2}{4S}}}{2\sqrt{\pi}S^{3/2}}. \tag{46}$$

The avalanche-size exponent is $\tau = 3/2$. The first moments are

$$\langle 1\rangle = 1, \quad \langle S\rangle = \delta w, \quad S_m^{\rm ABBM} := \frac{\langle S^2\rangle}{2\langle S\rangle} = m^{-4} + \frac{\delta w}{2}. \tag{47}$$

The duration distribution given a kick of size δw is

$$P_{\delta w}^T(T) = \exp\left(-\frac{\delta w m^4}{e^{Tm^2}-1}\right)\frac{\delta w m^6}{[2\sinh(Tm^2/2)]^2}. \tag{48}$$

This distribution is normalized. The first moments to leading order in δw are

$$\langle T\rangle = m^2[1 - \gamma_{\rm E} - \ln(m^4\delta w)] + \cdots, \tag{49}$$

$$\langle T^2\rangle = \frac{\pi^2}{3}\delta w + \cdots, \tag{50}$$

$$\langle T^3\rangle = 6\zeta(3)\frac{\delta w}{m^2} + \cdots, \tag{51}$$

$$\langle T^4\rangle = \frac{4\pi^4}{15}\frac{\delta w}{m^4} + \cdots, \tag{52}$$

$$T_m^{\rm ABBM} := \frac{\langle T^3\rangle}{3\langle T^2\rangle} = \frac{6\zeta(3)}{\pi^2 m^2} + \cdots = \frac{0.730763}{m^2} + \cdots. \tag{53}$$

B. The discretized particle model (DPM)

The discretized particle model (DPM) was introduced in Ref. [33]. There the reader finds a thorough discussion of its quasistatic properties, encompassing all three main universality classes of extreme-value statistics: Gumbel, Weibull, and Fréchet.

1. *Static quantities*

As we assume forces to be distributed according to

$$P_F(F) = \frac{e^{-F^2/2}}{\sqrt{2\pi}}, \tag{54}$$

this is the Gumbel class of Ref. [33] with $A = 1/2$, $\gamma = 2$, $\beta(x) = x^2/2$, and $\beta^{-1}(x) = \sqrt{2x}$. The name of this class stems from the fact that the blocking forces are distributed according to a *Gumbel* distribution ([33], Eq. (29), first line)

$$P_{\rm G}(a) = e^{-a}\Theta(a), \tag{55}$$

$$f = \sqrt{2}\sqrt{\ln(m^{-2}) - \ln(a)} \tag{56}$$

$$= f_{\rm c}^0 - \ln(a)\,m^2\rho_m + \cdots. \tag{57}$$

The constant $f_{\rm c}^0$, the scale ρ_m, and the exponent ζ are

$$f_{\rm c}^0 = \sqrt{2\ln(m^{-2})} + \mathcal{O}(m^{-1}), \quad \rho_m = \frac{1}{m^2\sqrt{2\ln(m^{-2})}}, \tag{58}$$

$$\zeta = 2^-. \tag{59}$$

By $\zeta = 2$ we mean $\rho_m \sim m^{-\zeta}$ with $\zeta = 2$. The growth of Eq. (58) with $1/m$ is slightly slower, reduced by the logarithm in Eq. (58), and denoted $\zeta = 2^-$.

The effective disorder force-force correlator reads

$$\Delta(w) = m^4 \rho_m^2 \tilde{\Delta}(w/\rho_m), \tag{60}$$

$$\tilde{\Delta}(w) = \frac{w^2}{2} + \mathrm{Li}_2(1 - e^w) + \frac{\pi^2}{6}. \tag{61}$$

The avalanche-size distribution for an infinitesimal kick was obtained in Ref. [33], where it was shown to be $P(S) \sim e^{-S/\rho_m}$. For a kick of size δw, this can be generalized to

$$P_{\delta w}^{\mathrm{DPM}}(S) = 4\delta w \sinh\left(\frac{1}{2\rho_m}\right)^2 e^{-S/\rho_m} \simeq \frac{\delta w}{\rho_m^2} e^{-S/\rho_m}. \tag{62}$$

Note that for the DPM the avalanche size S is discrete. The normalization is constructed such that the first moment of this discrete measure is $\langle S \rangle = \delta w$. This yields for the characteristic scale of avalanches

$$S_m = \frac{\langle S^2 \rangle}{2\langle S \rangle} = \frac{1}{2} \coth\left(\frac{1}{2\rho_m}\right) = \rho_m + \mathcal{O}(1/\rho_m). \tag{63}$$

2. Dynamic quantities

The DPM defined in Ref. [33] advances instantaneously. The easiest way to endow it with a realistic dynamics is to consider the Langevin equation (1). If the disorder is needle-like as on the right of Fig. 2 (the original construction of [33]), then either the particle is at rest blocked by a needle, or it moves, and the only force acting on it comes from the spring. Neglecting that the spring gets shorter during the movement, the response function is given by $R(t) \sim P(S/v)$, where $v = f_c$, resulting in

$$R^{\mathrm{DPM}}(t) = \tau_m^{-1} e^{-t/\tau_m}, \quad \tau_m = \frac{\rho_m}{f_c} = \frac{1}{2m^2 \ln(m^{-2})}. \tag{64}$$

Stated differently, the velocity distribution is

$$P^{\mathrm{DPM}}(\dot{u}) = \delta(\dot{u} - f_c). \tag{65}$$

As a consequence, the distribution of durations T, given a kick δw, can be obtained from the avalanche-size distribution as

$$P_{\delta w}^{\mathrm{DPM}}(T) \simeq \frac{\delta w}{\rho_m \tau_m} e^{-T/\tau_m}. \tag{66}$$

III. NUMERICAL RESULTS

A. Critical force

First one integrates the equation of motion (1), with forces as given by Eq. (5). This gives $u(t)$, or u_w as a function of the external point $w = vt$, defined such that $u_w = u(t)$. Example trajectories for $u_w - w$, $\dot{u}_w - v$, and F_w are plotted in Figs. 4–6.

It is important to note that the position u_w and force F_w are related, since Eq. (1) yields, after averaging over time,

$$\overline{\partial_t u(t)} = v = m^2 \overline{[w - u(t)]} + \overline{F(t)}. \tag{67}$$

Note that the overline, defined as an average over disorder realizations, can be performed as an average over time when driving the system at a finite velocity $v > 0$. For the discretized particle model, the critical force was computed analytically in Ref. [33]. It is given by Eqs. (55)–(56):

$$f_c(m) := \langle f \rangle_{\mathrm{G}} = \sqrt{2} \int_0^{m^{-2}} \sqrt{\ln(m^{-2}) - \ln(a)}\, e^{-a}\, da. \tag{68}$$

Expanding for small m, we find

$$f_c(m) = f_c^0 + \frac{\gamma_{\mathrm{E}}}{f_c^0} - \frac{\frac{\gamma_{\mathrm{E}}^2}{2} + \frac{\pi^2}{12}}{(f_c^0)^3} + \frac{2\gamma_{\mathrm{E}}^3 + \gamma_{\mathrm{E}}\pi^2 - 2\psi''(1)}{4(f_c^0)^5} + \cdots, \tag{69}$$

$$f_c^0 = \sqrt{2\ln(m^{-2})}. \tag{70}$$

In Fig. 7 we compare the measured critical force for the Ornstein-Uhlenbeck model, $f_c^{\mathrm{OU}} \equiv m^2[w - u(w)] - v$, to the critical force (69) predicted by the particle model. We find that they agree, up to a constant

$$f_c^{\mathrm{OU}} \simeq f_c(m) - 0.35. \tag{71}$$

This constant is not surprising, as the microscopic disorder of the Ornstein-Uhlenbeck process is different from the DPM,

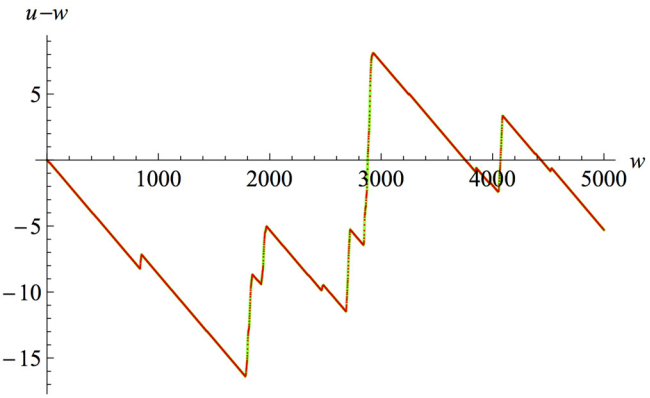

FIG. 4. $u_w - w$ for $\delta t = 10^{-4}$, $v = 0.1$, $m^2 = 0.1$, INS. See Appendix B for implementation details. Red points are data points equally spaced in time, the green line between them is an interpolation.

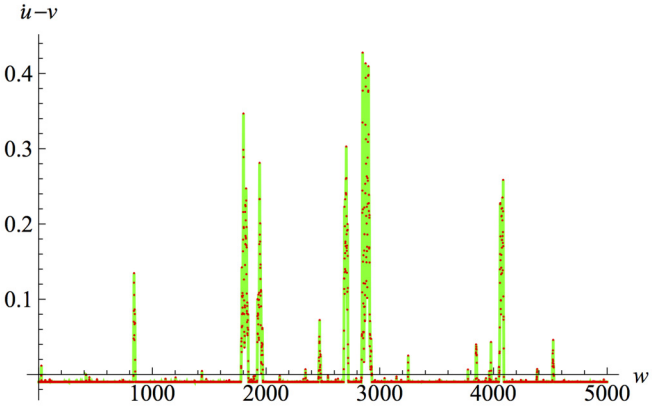

FIG. 5. $\dot{u}(w) - v$ with the same parameters as in Fig. 4.

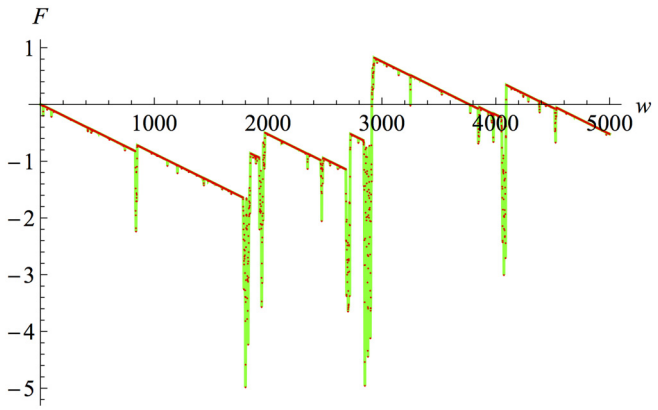

FIG. 6. $F(w)$ with the same parameters as in Fig. 4.

and the critical force is not universal. We note that the reported value 0.35 is almost the correlation $e^{-1} \approx 0.368$ of the Ornstein-Uhlenbeck process at distance $u = 1$.

B. Velocity distribution

In the discretized-force model, and supposing that the forces remain constant between integers, the velocity distribution between sites u and $u+1$ is given by

$$P_u(\dot{u}) = \langle P_F(f - \dot{u})\rangle_{\mathrm{G}}. \tag{72}$$

Here $P_F(f)$ is the initial force distribution (54), and the average is over the Gumbel distribution defined by Eqs. (55)–(56). As we are interested in the velocity distribution sampled equally in time and not in space, we still have to multiply with $v/\dot{u}$, resulting in

$$\begin{aligned} P_t(\dot{u}) &= \frac{v}{\dot{u}} P_u(\dot{u}) \\ &= \frac{v}{\dot{u}} \frac{1}{\sqrt{2\pi}} \int_0^{m^{-2}} e^{-\left(\frac{\dot{u}}{\sqrt{2}} - \sqrt{\ln(m^{-2}) - \ln(a)}\right)^2} e^{-a}\, da. \end{aligned} \tag{73}$$

This formula, evaluated numerically, is compared to simulations for $m^2 = 10^{-3}$ in Fig. 8. While the tail is correctly predicted, the amplitude for small $\dot{u}$ is underestimated. This

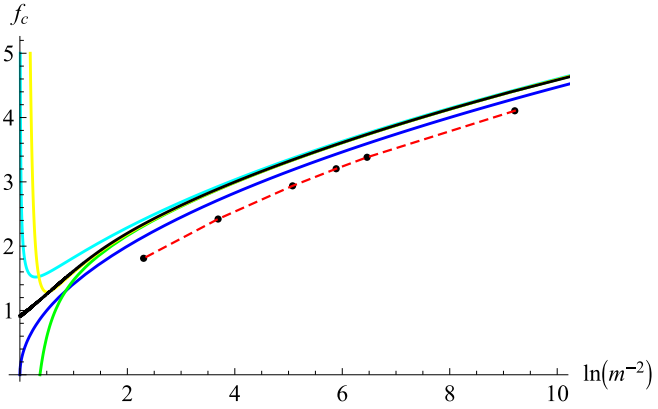

FIG. 7. The critical force f_c as a function of m. Thick black curve: the results of the integral (68). The small-m expansion is in blue, cyan, green, and yellow. The data points are from our numerical simulation. (DNS, $\delta u = 10^{-2}$, $\delta t = 10^{-4}$, $N = 3 \times 10^6$.)

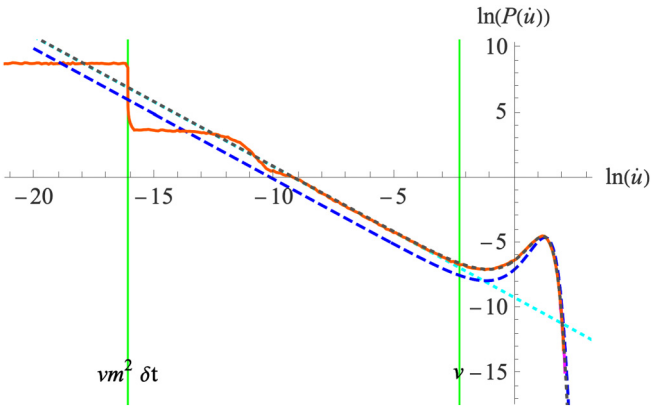

FIG. 8. $P(\dot{u})$ for $m^2 = 10^{-3}$ (orange solid line). The blue dashed curve is given by Eq. (73); the gray dotted one by the same formula, replacing $m^{-2} \to 0.39m^{-2}$, yields a perfect fit. The cyan dotted line is the result for ABBM, Eq. (44). (INS, $\delta t = 10^{-3}$, $v = 0.1$, $N = 5 \times 10^8$.)

is related to the underestimation of f_c reported in Eq. (71). Indeed, we find a perfect fit for $m^2 = 10^{-3}$ under the replacement $m^{-2} \to 0.39m^{-2}$; see Fig. 8.

C. The response function

1. Measurement prescription

The response function plays a key role as it enters into the rounding of the cusp, and we need to measure it to verify the prediction in Eq. (64). To this aim, we let the system relax to $\dot{u} = 0$ and then kick it at time $t = t_{\mathrm{kick}}$, moving the center of the well from w to $w + \delta w$. The nonlinear response function is then given by

$$R(t|\delta w) := \frac{\langle \dot{u}(t + t_{\mathrm{kick}})\rangle}{\delta w}. \tag{74}$$

The linear response is the limit of a small kick δw,

$$R(t) := \lim_{\delta w \to 0} R(t|\delta w). \tag{75}$$

In practice, δw can be chosen finite; we give suitable values in Figs. 9 and 10. The response function is normalized, and its first moment defines a characteristic timescale τ,

$$\int_0^\infty R(t)\, dt = 1, \quad \tau := \langle t\rangle = \int_0^\infty t\, R(t)\, dt. \tag{76}$$

Comparing the measured timescale $\tau := \langle t\rangle$ to the predicted one τ_m from Eq. (64) is an important check of the theory.

2. Response function for DPM

We start with the response function for the discretized force model of Ref. [33]. In Fig. 9 we show a numerical verification for the analytic prediction in Eq. (64). Already for a rather large mass of $m^2 = 10^{-2}$ the agreement between theory and simulation is rather good.

3. Response function for Ornstein-Uhlenbeck forces

In Fig. 10 we show the response function for Ornstein-Uhlenbeck forces. While for the DPM, which has needlelike disorder, the response function in Fig. 9 had already converged

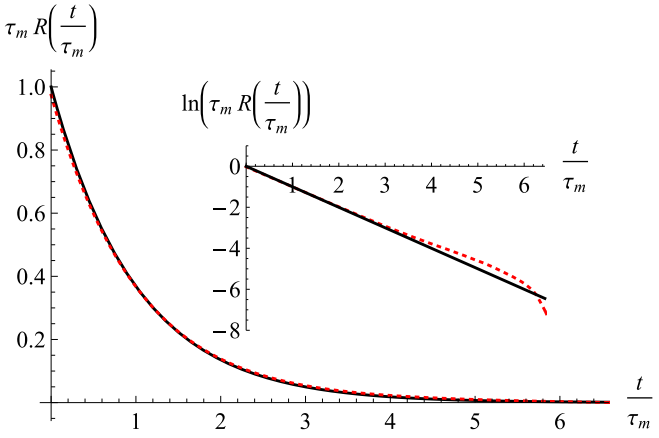

FIG. 9. The response function for the discretized force model (needle disorder) for $m^2 = 10^{-2}$ (blue). The red dashed curve is an exponential function with timescale τ_m as given by Eq. (64). Inset: the same for $\ln R(t)$. (DNS, $\delta t = 10^{-4}$, $\delta w = 0.1$.)

to the asymptotic behavior of Eq. (64) for $m^2 = 10^{-2}$, the convergence for Ornstein-Uhlenbeck forces is much slower, and one has to go to $m^2 = 10^{-5}$ to reach a similar agreement, albeit with a noticeable difference in the timescale $\tau = \langle t \rangle$. The rather slow convergence [43] is shown in the inset of Fig. 10. A second observation is that the response function $R(t)$ for $t \to 0$ starts at $1/\tau_{\mathrm{ABBM}} = m^2$. This is a consequence of the continuity of $F(u)$: Since in the beginning $m^2[w - u(t)] + F(u(t)) = 0$, the response function is that of the free theory, itself equivalent to that of the ABBM model,

$$R(t) \approx R_{\mathrm{free}}(t) \equiv R_{\mathrm{ABBM}}(t) = m^2 e^{-m^2 t}\Theta(t). \tag{77}$$

The position $u(t)$ then increases, and since pinning occurs at maxima of $F(u)$, most likely $F(u)$ decreases, leading to an increase in $\dot{u}$ as compared to the free theory. When $u(t) -$

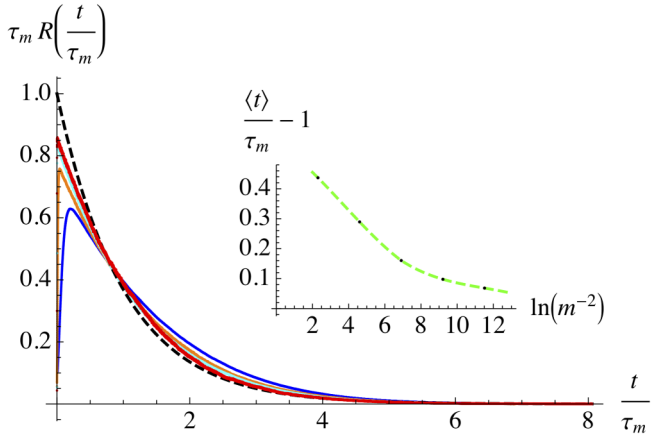

FIG. 10. The response function for the Ornstein-Uhlenbeck process: the analytical result is the black dashed curve. Numerical results from bottom to top are for $m^2 = 10^{-2}$ (blue), $m^2 = 10^{-3}$ (orange), $m^2 = 10^{-4}$ (cyan), and $m^2 = 10^{-5}$ (red). DNS, $\delta t = 10^{-4}$, $N = 10^8$. The two larger masses have $\delta w = 0.1$ and $\delta u = 10^{-6}$, the two smaller ones $\delta w = 1$ and $\delta u = 10^{-4}$. Inset: The measured timescale $\langle t \rangle$ (dots) compared to the prediction for τ_m in Eq. (64).

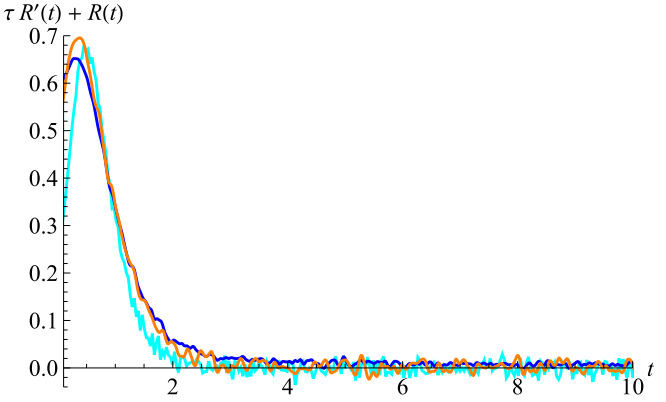

FIG. 11. The function $\delta_{\mathrm{BL}}(t) := (\tau\partial_t + 1)R(t)$ for the measured response function with $m^2 = 10^{-2}$ (blue), $m^2 = 10^{-3}$ (orange), $m^2 = 10^{-4}$ (cyan). Parameters as in Fig. 10, except $N = 2 \times 10^8$ for $m^2 = 10^{-4}$.

$u(t_{\mathrm{kick}}) \simeq 1$, we expect the forces $F(u)$ to be decorrelated from their initial value. This estimates the boundary layer in u as $\delta u \approx 1$. It is nontrivial to predict the boundary layer in t, i.e., the region in which $R(t)$ rises, before decaying approximately as an exponential. After some experimentation, we found that this can be extracted by plotting the combination

$$\delta_{\mathrm{BL}}(t) := (\tau\partial_t + 1)R(t) \tag{78}$$

appearing in Eq. (31), with τ defined in Eq. (76). By construction

$$\int_0^\infty dt\, R(t) = \int_0^\infty dt\, \delta_{\mathrm{BL}}(t) = 1. \tag{79}$$

If $R(t)$ is exponentially decaying, $\delta_{\mathrm{BL}}(t)$ equals $\delta(t)$. Deviations lead to a smeared-out δ function. In Fig. 11 we show $\delta_{\mathrm{BL}}(t)$ for several masses and timescales ranging from $\tau \approx 14$ to $\tau \approx 596$. Despite the enormous range of timescales, the resulting $\delta_{\mathrm{BL}}(t)$ is almost independent of τ, and decays to zero on a range of $\delta t \approx 2$. We believe that this function could be extracted from extreme-value statistics, by considering the statistics of a Brownian motion close to one of its records. It is, e.g., known that the fractal dimension of the record set, i.e., the position when the movement of the particle stops again, is 1/2 [44,45].

4. The response function at a finite driving velocity

The response function at a finite driving velocity and the associated timescales are defined as

$$R_v(t) := \lim_{\delta w \to 0} \frac{1}{\delta w}\left[\langle \dot{u}(t)\rangle_v^{\delta w} - v\right], \tag{80}$$

$$\langle t \rangle_v = \int_0^\infty dt\, R_v(t) t. \tag{81}$$

The expectation value on the r.h.s. of Eq. (80) is the expectation of $\dot{u}(t)$, given a driving velocity v and an additional kick at time $t = 0$; we have subtracted the expectation without a kick, $\langle \dot{u}(t)\rangle_v^{\delta w = 0} = v$. The timescale $\langle t \rangle_v$ defined in Eq. (81) should then behave as

$$\frac{1}{\langle t \rangle_v} \simeq f_c - v, \quad v \text{ small}. \tag{82}$$

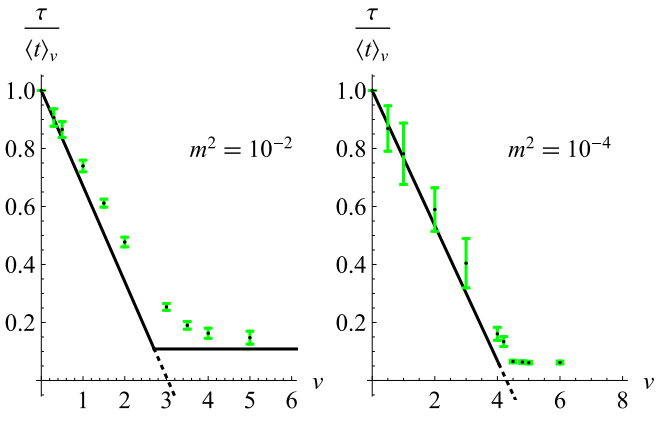

FIG. 12. Inverse of the measured timescale $\langle t\rangle_v := \int_0^\infty dt\, t R_v(t)$, as a function of v. The data points are given with 99% confidence intervals (green). Superimposed are the two analytical curves (81), valid for $v \leqslant f_c$, and (82), valid for $v \geqslant f_c$. (DNS, $\delta t = 10^{-4}$, $\delta u = 10^{-6}$ for $m^2 = 0.01$, and $\delta u = 10^{-4}$ for $m^2 = 10^{-4}$.)

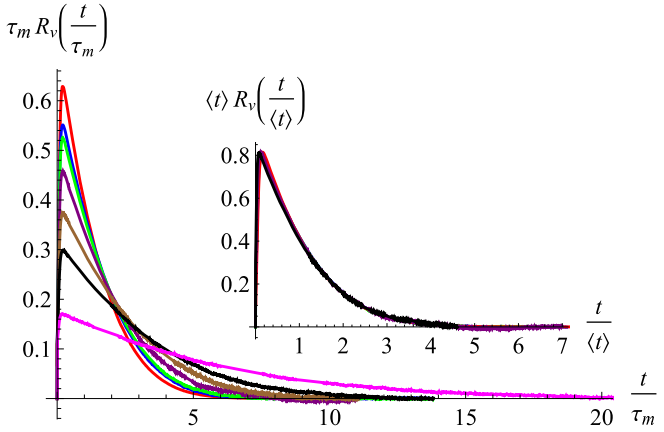

FIG. 13. Main plot: The response function rescaled with the theoretically predicted timescale τ_m. Velocities from top to bottom are $v = 0$ (red), $v = 0.3$ (blue), $v = 0.5$ (green), $v = 1$ (violet), $v = 1.5$ (brown), $v = 2$ (black), and $v = 3 \approx f_c$ (magenta). Inset: Scaling collapse for the velocities $v \leqslant 2$, using the measured timescale $\langle t\rangle$ instead of τ_m for the rescaling. (DNS, $\delta u = 10^{-6}$, $\delta t = 10^{-4}$, $N = 10^7$.)

What appears on the r.h.s. is the relative velocity between the "ballistically" moving particle as given by Eq. (65) and the advancement of the confining potential. On the other hand, at large driving velocity, the disorder acts as a thermal noise, and the response function reduces to that of the free theory, equivalent to that of the ABBM model, resulting in

$$\frac{1}{\langle t\rangle_v} \simeq \tau_{\text{ABBM}}^{-1} = m^2, \quad v \text{ large}. \tag{83}$$

These two curves are plotted in Fig. 12. They intersect at $v = f_c - m^2$. Intuitively we expect the transition to take place at $v = f_c$, and to be smoothed out due to the finite width of the velocity distribution (73). As we can see in Fig. 12, the transition gets sharper when m^2 decreases. A phase transition at $v = f_c$ is expected in the limit of $m^2 \to 0$.

Our final observation is that the timescale $\langle t\rangle_v$ defined in Eq. (82) can be used for a scaling collapse of the response functions $R_v(t)$ defined in Eq. (80); see Fig. 13. Details of the analysis are given in Ref. [43].

D. Avalanche-size distribution

The avalanche-size distribution is shown in Fig. 1, for $m^2 = 10^{-4}$, overlayed with two theoretical curves: the kicked ABBM model as given in Eq. (46) (bright dotted cyan), and the DPM given in Eq. (62) (dark blue dashed).

For small S, one sees the $S^{-3/2}$ behavior characteristic for ABBM coincide with the theoretical curve (46) (cyan dashed). For large S, this crosses over to the prediction of Eq. (62) for the DPM with avalanche exponent $\tau = 0$ (blue dashed). Note that there are no adjustable parameters, and both curves respect their own normalizations. The crossover takes place at $S \approx 1$, and extends over about half a decade in both directions.

E. Avalanche-duration distribution

The avalanche-duration distribution is shown in Fig. 14, superimposed with the two theoretical predictions (48) for ABBM (cyan dotted) and (66) for the DPM (blue dashed). The simulations agree very well with ABBM for small times, while the overall weight for large times is seemingly overestimated in Eq. (66), contrary to what one saw in Fig. 1 for the avalanche-size distribution. Normalization issues are more pronounced since the singularity for small times, $P(T) \sim T^{-2}$, is stronger than the $P(S) \sim S^{-3/2}$ for the avalanche size. Another reason for the slow convergence is the relatively broad avalanche-velocity distribution, assumed to be restricted to $\dot{u} = f_c$ in the derivation of Eq. (48).

F. Correlators $\Delta_v(w)$, $\Delta_{\dot{u}}(w)$, $\Delta_F(w)$

In Sec. I B 5, we defined the three correlation functions $\Delta_v(w)$, $\Delta_{\dot{u}}(w)$, and $\Delta_F(w)$, which are the correlations of three forces: confining well, friction, and disorder. Since they add up to zero, two variables are independent, and one would expect three independent correlation functions, which are most symmetrically expressed as $\Delta_v(w)$, $\Delta_{\dot{u}}(w)$, and $\Delta_F(w)$. This expectation is incorrect: there are only two independent

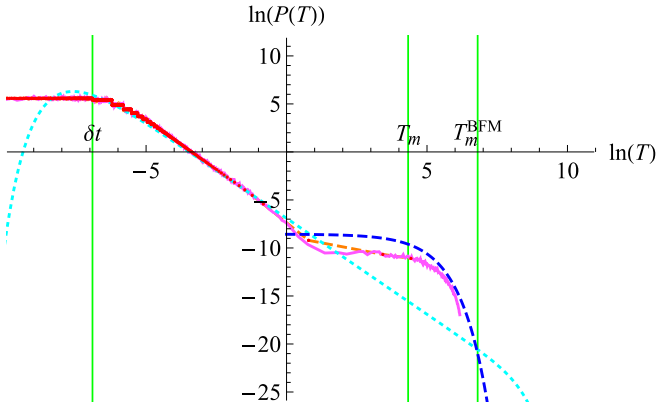

FIG. 14. $P(T)$ measured numerically via INS for $m^2 = 10^{-3}$, ($\delta w = 1$, $\delta t = 10^{-3}$, $N = 5 \times 10^8$). This is compared to the theory prediction (48) for ABBM (cyan dotted), and (66) for DPM (blue dashed).

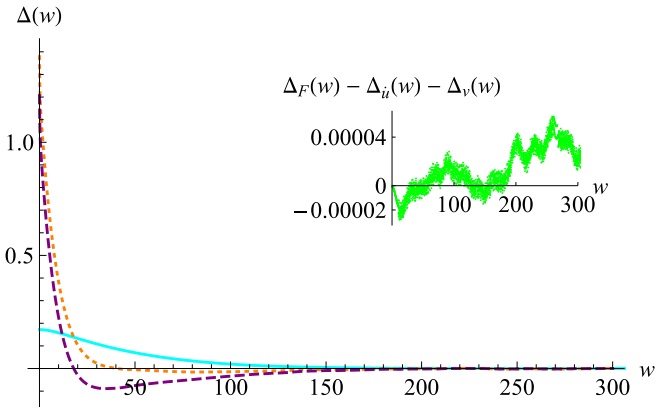

FIG. 15. The measured Δ_v (cyan), Δ_F (orange dashed), and $\Delta_{\dot u}$ (purple dotted) for $m^2 = 0.01$ at $v = 0.5$. The inset shows that the difference $\Delta_F - \Delta_v - \Delta_{\dot u}$ vanishes. (DNS, $\delta u = 0.01$, $\delta t = 10^{-4}$, $N = 10^8$.)

quantities, summarized in the relation

$$\Delta_v(w) + \Delta_{\dot u}(w) = \Delta_F(w). \tag{84}$$

A numerical verification is presented in Fig. 15. An analytical proof can be given too: identifying $w \equiv vt$, one has

$$\begin{aligned}\Delta_F(w-w') &= \langle F_w F_{w'}\rangle^{\rm c}\\ &= \langle [\dot u_w + m^2(u_w - w)][\dot u_{w'} + m^2(u_{w'} - w')]\rangle^{\rm c}\\ &= \langle \dot u_w \dot u_{w'}\rangle^{\rm c} + m^4\langle (u_w - w)(u_{w'} - w')\rangle^{\rm c}\\ &\quad + m^2\langle \dot u_w(u_{w'} - w') + (u_w - w)\dot u_w\rangle^{\rm c}.\end{aligned} \tag{85}$$

The last term can be written as

$$\begin{aligned}&\langle \dot u_w(u_{w'} - w') + (u_w - w)\dot u_w\rangle^{\rm c}\\ &\quad = (\partial_t + \partial_t')\langle (u_w - w)(u_{w'} - w')\rangle^{\rm c}\\ &\quad = \frac{1}{v}(\partial_w + \partial_w')\Delta_v(w - w') = 0.\end{aligned} \tag{86}$$

This proves Eq. (84).

In Fig. 16, we find numerically satisfied another relation,

$$m^4\Delta_{\dot u}(w) = -v^2\partial_w^2\Delta_v(w). \tag{87}$$

This relation expresses the time derivative of $u(t) = u_w$ by its dependence on $w = vt$: $\partial_t u(t) = v\partial_w u_w$. Thus knowing $\Delta_v(w)$ is enough, and the two other quantities can be expressed as

$$\Delta_{\dot u}(w) = -\frac{v^2}{m^4}\Delta_v''(w), \tag{88}$$

$$\Delta_F(w) = \Delta_v(w) - \frac{v^2}{m^4}\Delta_v''(w). \tag{89}$$

Knowing $\Delta_v(w)$ it is easy to find $\Delta_{\dot u}(w)$ by taking two derivatives. It is already less obvious to reconstruct $\Delta_v(w)$ from $\Delta_{\dot u}(w)$, as this procedure involves two integration constants. In principle the latter are fixed since all correlations vanish for $w \to \infty$; in practice, however, fluctuations grow with increasing w, and they show up in the two integration constants. It is even more involved to reconstruct $\Delta_v(w)$ from $\Delta_F(w)$:

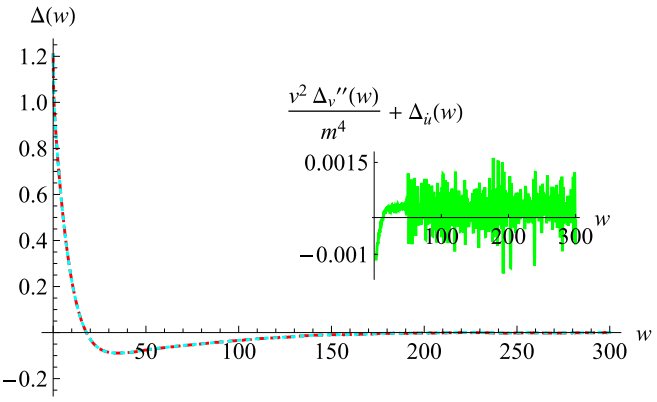

FIG. 16. Numerical test of Eq. (88) for $m^2 = 10^{-2}$, $v = 0.5$. Plotted are $\Delta_{\dot u}(w)$ (cyan dotted) and $-\frac{v^2}{m^4}\Delta_v''(w)$ (red dashed). The inset shows the difference. (DNS, $\delta u = 0.01$, $\delta t = 10^{-4}$, $N = 10^8$.)

Formally, this can be achieved by the series

$$\Delta_v(w) = \sum_{n=0}^{\infty}\left[\frac{v}{m^2}\frac{d}{dw}\right]^{2n}\Delta_F(w). \tag{90}$$

As it is rather badly converging, it may well be useless in practice.

G. Measuring $\Delta(w)$ at vanishing driving velocity

In an experiment, it is difficult to measure $\Delta(w) = \lim_{v\to 0}\Delta_v(w)$. In our simulation, we can do this: We move the parabola from $w \to w + \delta w$, and then wait until the dynamics cedes. Due to Middleton's theorem [46], the position u_w is history independent. From u_w we obtain $\Delta(w)$ via formula (17). The DPM [33] predicts that

$$\Delta(w) = m^4\rho_m^2\tilde\Delta(w/\rho_m), \tag{91}$$

$$\tilde\Delta(w) = {\rm Li}_2(1 - e^{|w|}) + \frac{w^2}{2} + \frac{\pi^2}{6}. \tag{92}$$

To check this relation, we study the experimentally measured $\Delta_{\rm exp}(w)$, and then invert Eq. (91) to obtain

$$\tilde\Delta_{\rm exp}(w) = \frac{1}{m^4\rho_m^2}\Delta_{\rm exp}(w/\rho_m). \tag{93}$$

Figure 17 shows convergence against the theoretical result.

H. The disorder correlator $\Delta_v(w)$ at a finite driving velocity

For a finite driving velocity, Eq. (20) predicts that the measured $\Delta_v(w)$ is obtained from the zero-velocity correlator $\Delta(w)$ by folding with two response functions. In the inset of Fig. 18 we check that this construction works for $v = 0.5$, by folding the numerically measured zero-velocity correlator $\Delta(w)$ with the numerically measured zero-velocity response function $R(t)$.

We numerically established that the response function evolves with v from their zero-velocity limit (see Fig. 13), and the same may happen for the effective disorder correlator, technically the effective action of the theory. While the agreement shown in Fig. 18 should be sufficient for a typical experiment, the question arises what happens when we

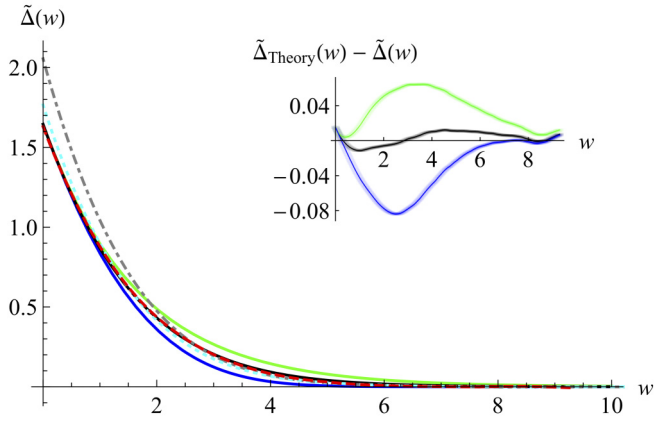

FIG. 17. Convergence of the measured $\tilde{\Delta}(w)$ for $m^2 = 10^{-2}$ (gray dot-dashed), $m^2 = 10^{-3}$ (cyan dotted), and $m^2 = 10^{-4}$ (red dashed). This is compared to three theoretical curves: an exponential function with the same slope at $w = 0$ (green, top curve), Eq. (92) (black, middle curve), and the one-loop functional renormalization group result (blue, bottom curve); see Eqs. (4.5) and (4.11) of [23]. The inset shows the difference of the measured $\tilde{\Delta}(w)$ at $m^2 = 10^{-4}$ and the theoretical curves in their respective colors, together with error bars at a 99% confidence level. (DNS, $\delta u = 0.01$, $\delta t = 10^{-4}$, $N = 10^8$, $\delta w = 0.1$.).

increase the driving velocity. Intuitively, as for the response function, we expect a transition when the driving velocity exceeds f_c.

I. Reconstructing $\Delta(w)$ from $\Delta_v(w)$

In Secs. I B 2 to I B 4 we proposed two procedures to reconstruct the zero-velocity correlator $\Delta(w)$, based either on a boundary-layer analysis (Sec. I B 2) or a differential equation (Sec. I B 4). These methods contain a parameter, the timescale τ of the response function, in the combination $\delta_w = \tau v$, and allow us to extract the latter if unknown. Let us analyze these methods in turn.

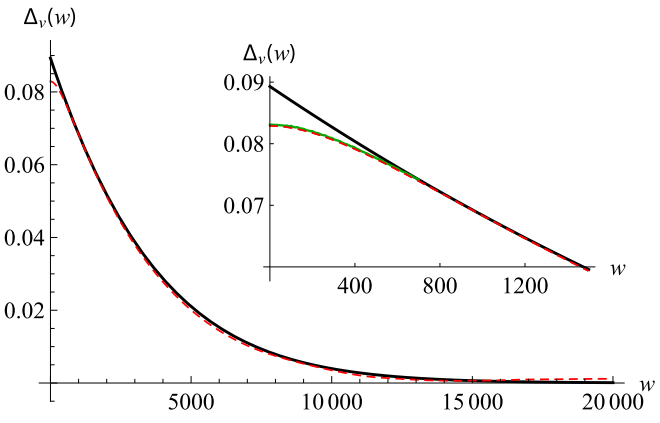

FIG. 18. The numerically measured $\Delta_v(w)$ for $v = 0.5$ (red dashed, with 95%-confidence intervals shaded red) as defined in Eq. (18). For $w > 1000$ it agrees well with the theoretical prediction (91) (black solid). The inset shows the same curves, superimposed with the theoretical prediction (91) folded according to Eq. (20) with the numerically measured response function (green), lying underneath $\Delta_v(w)$ obtained numerically (red dashed). (DNS, $\delta u = 0.01$, $\delta t = 10^{-4}$, $N = 10^7$.)

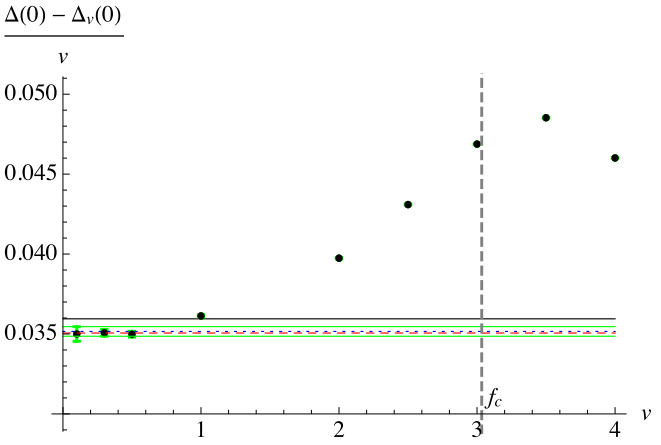

FIG. 19. The measured amplitude of the rounding $v^{-1}[\Delta_{v=0}(0) - \Delta_v(0)]$ for $m^2 = 0.01$ and $v = 0.1, 0.3, 0.5, 1, 2, 3.5, 4$; $f_c \simeq 3.035$. Error bars (green) are included in the fit and represent 99% confidence intervals on the data. We compare several curves. In black is shown the prediction from Eq. (22) with $\tau = \tau_m$, and $\Delta'(0^+)$ as given by Eq. (91). In blue is the prediction from Eq. (22) with $\tau = \langle t \rangle$, and $\Delta'(0^+)$ as measured in the simulation, accompanied by error bars in green. In red is a weighted fit to the velocities $v \leqslant 0.5$, verifying Eq. (22) with a relative precision of 3×10^{-3}. Note the transition at $v = f_c$. (DNS, $\delta u = 0.01$, $\delta t = 10^{-4}$, $N = 10^8$.)

1. Boundary-layer analysis

As proposed in Sec. I B 2, we use the boundary-layer formula (27) to plot in Fig. 20 the measured $\Delta_v(w)$ against $\tilde{w} = \sqrt{w^2 + \delta_w^2}$, $\delta_w = v\tau$, using the timescale $\tau = \langle t \rangle$ measured from the response function. By extrapolation to $\tilde{w} = 0$ we obtain the full $\Delta(w)$. This works decently well, especially for the smaller driving velocity $v = 0.1$.

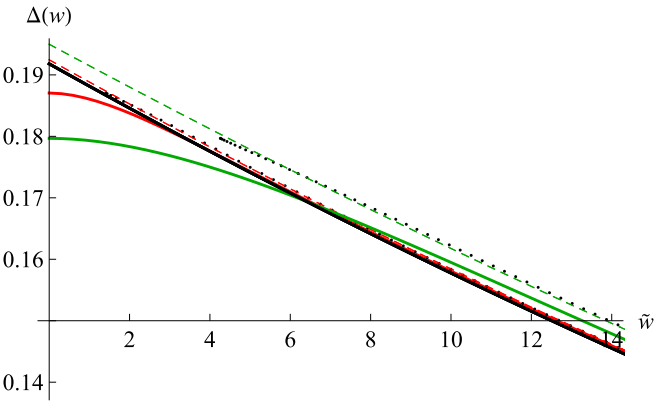

FIG. 20. Measurement of $\Delta_v(w)$ for $v = 0$ (solid blue, top), $v = 0.1$ (solid red, middle), and $v = 0.3$ (solid green, bottom). We show unfolding via a boundary layer analysis, using $\tau := \langle t \rangle = 14.08$ as measured for the response function, both for $v = 0.1$ (black dots), prolonged to zero (red dashed), and $v = 0.3$ (black dots), prolonged to zero (green dashed). The variable $\tilde{w} = \sqrt{w^2 + (\tau v)^2}$. (DNS, $\delta t = 10^{-4}$, $\delta u = 10^{-2}$, $N = 10^8$.)

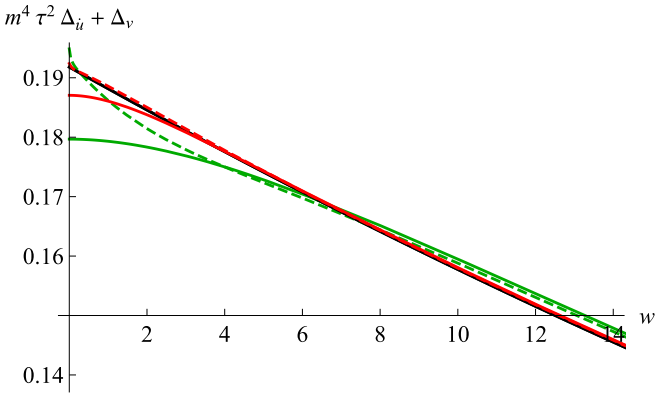

FIG. 21. Measurement of $\Delta_v(w)$ for $v = 0$ (solid blue, top), $v = 0.1$ (solid red, middle), and $v = 0.3$ (solid green, bottom). We show unfolding via the differential equation (34) using $\tau := \langle t \rangle = 14.08$ as measured for the response function, both for $v = 0.1$ (red dashed) and $v = 0.3$ (green dotted). (DNS, $\delta t = 10^{-4}$, $\delta u = 10^{-2}$, $N = 10^8$.)

2. Differential equation

A second unfolding procedure was proposed in Sec. I B 4. Repeating the analysis performed in Fig. 20, we show in Fig. 21 the reconstructed $\Delta(w)$. For $v = 0.1$ the unfolding procedure reproduces the $v = 0$ correlator with high precision. The agreement is not as good for $v = 0.3$.

3. Reconstructing the timescale τ

In the last two sections, we tested the reconstruction procedures under the assumption that the timescale τ was known from an independent measurement of the response function. In practice, τ may not be available. In that case, we try to find $\delta_w = v\tau$, which best removes the curvature of $\Delta_v(w)$. The estimated values for τ are reported in Table II, together with an estimate of τ from Eq. (30). While the latter gives only fair results, both reconstruction procedures allow us to extract the time scale τ rather precisely.

IV. SUMMARY AND CONCLUSION

We have shown that there is more to mean-field theory than replacing the effective force landscape by a random walk (ABBM model). As forces cannot grow unboundedly, they must finally saturate, leading to a different regime of uncorrelated forces (DPM). Above we propose to describe the crossover by modeling forces as an Ornstein-Uhlenbeck process. Using numerical simulations supported by analytical results for all key ingredients, we quantify the signatures expected in experiments. The key observable is the effective force-force correlator, which is readily accessible in experiments. As experiments necessitate a finite driving velocity, the measured signal is always smeared out. Above we developed and tested procedures to reconstruct the zero-velocity response and force-force correlations from finite-velocity measurements. We have already tested our procedure with success for magnetic domain walls (collaboration with G. Durin) and knits (collaboration with A. Douin and F. Lechenault). Each of these systems has its own peculiarities, on which we will report in forthcoming publications.

ACKNOWLEDGMENTS

It is a pleasure to thank A. Kolton, G. Mukerjee, A. Rosso, and B. Walter for fruitful discussions. The questions raised here are inspired by our ongoing collaboration with experimentalists and we are grateful for the inspirations brought to us by G. Durin (magnetic domain walls) as well as A. Douin and F. Lechenault (knitting).

APPENDIX A: CORRELATIONS OF AN ORNSTEIN-UHLENBCK PROCESS

Suppose that

$$\partial_u F(u) = -F(u) + \xi(u). \tag{A1}$$

This equation is solved by

$$F(u) = \int_{-\infty}^{u} du_1\, e^{-(u-u_1)}\xi(u_1). \tag{A2}$$

It leads to microscopic correlations

$$\begin{aligned}\Delta(u-u') &:= \overline{F(u)F(u')} \\ &= \int_{-\infty}^{u} du_1 \int_{-\infty}^{u'} du_2\, e^{-(u+u'-u_1-u_2)}\overline{\xi(u_1)\xi(u_2)} \\ &= 2\int_{-\infty}^{\min(u,u')} d\tilde u\, e^{-(u+u'-2\tilde u)} \\ &= e^{-|u-u'|}.\end{aligned} \tag{A3}$$

APPENDIX B: NUMERICAL IMPLEMENTATIONS

We used several numerical implementations:

(i) *Direct numerical simulation (DNS).* To solve the coupled set of differential equations (1)–(3) we use a space discretization $\delta u = 10^{-6}$ to 10^{-2} (depending on m) to first obtain the random forces $F(u)$ for $u = n\delta u$, $n \in \mathbb{N}$. $F(u)$ is then linearly interpolated between these points. We finally solve Eq. (1) with the Euler method, using a time discretization of $\delta t = 10^{-4}$.

TABLE II. Comparison of the measured timescale τ and its estimation using the methods of Secs. I B 2–I B 4. The estimation via the differential equation (27) is the most precise, followed by the boundary-layer analysis using Eq. (34), whereas the approximation (30) has a relatively large error.

Parameters	$\tau := \int_t tR(t)$	τ from boundary layer analysis via Eq. (27)	τ from differential Eq. (34)	τ from Eq. (30)
$m^2 = 0.01$, $v = 0.1$	14.08	14.10	14.08	14.87
$m^2 = 0.01$, $v = 0.3$	14.08	14.08	14.08	13.90
$m^2 = 10^{-4}$, $v = 0.5$	596	587	587	664

(ii) *Improved numerical solver (INS)*. In the coupled equations of motion (1)–(3), the force $\mathcal{F}(t) := F(u(t))$ can statistically equivalently be modeled as [47–49]

$$\partial_t \mathcal{F}(t) = -\mathcal{F}(t) + \sqrt{\dot{u}(t)}\eta(t), \tag{B1}$$

$$\langle \eta(t)\eta(t')\rangle = 2\delta(t). \tag{B2}$$

The advantage of this scheme is that there is only one parameter, namely the time discretization δt, but none for the space discretization δu. The effective space discretization is $\delta u \approx \dot{u}(t)\,\delta t$, thus is finer when the system moves slowly. Treating the multiplicative noise of Eq. (B1) however demands some care [50]. We use both a direct simulation with a very small time step, and the scheme proposed in [47] and tested in [48,49].

The number of samples is denoted

$$N := \text{number of samples}. \tag{B3}$$

Most of our results were verified with both schemes, DNS and INS.

[1] P. Le Doussal, K. J. Wiese, S. Moulinet, and E. Rolley, Height fluctuations of a contact line: A direct measurement of the renormalized disorder correlator, Europhys. Lett. **87**, 56001 (2009).

[2] J. S. Urbach, R. C. Madison, and J. T. Markert, Interface Depinning, Self-Organized Criticality, and the Barkhausen Effect, Phys. Rev. Lett. **75**, 276 (1995).

[3] G. Durin and S. Zapperi, Scaling Exponents for Barkhausen Avalanches in Polycrystalline and Amorphous Ferromagnets, Phys. Rev. Lett. **84**, 4705 (2000).

[4] D.-H. Kim, S.-B. Choe and Sung-Chul Shin, Direct Observation of Barkhausen Avalanche in Co Thin Films, Phys. Rev. Lett. **90**, 087203 (2003).

[5] G. Durin and S. Zapperi, The Barkhausen effect, in *The Science of Hysteresis*, edited by G. Bertotti (Academic, Amsterdam, 2006), p. 51.

[6] S. Lemerle, J. Ferré, C. Chappert, V. Mathet, T. Giamarchi, and P. Le Doussal, Domain Wall Creep in an Ising Ultrathin Magnetic Film, Phys. Rev. Lett. **80**, 849 (1998).

[7] E. A. Jagla and A. B. Kolton, The mechanisms of spatial and temporal earthquake clustering, J. Geophys. Res. **115**, B5 (2009).

[8] Y. Y. Kagan, Seismic moment distribution revisited: I. Statistical results, Geophys. J. Int. **148**, 520 (2002).

[9] D. S. Fisher, Collective transport in random media: From superconductors to earthquakes, Phys. Rep. **301**, 113 (1998).

[10] D. Fisher, K. Dahmen, S. Ramanathan, and Y. Ben-Zion, Statistics of Earthquakes in Simple Models of Heterogeneous Faults, Phys. Rev. Lett. **78**, 4885 (1997).

[11] M. Paczuski and S. Boettcher, Universality in Sandpiles, Interface Depinning, and Earthquake Models, Phys. Rev. Lett. **77**, 111 (1996).

[12] Y. Ben-Zion and J. R. Rice, Earthquake failure sequences along a cellular fault zone in a three-dimensional elastic solid containing asperity and nonasperity regions, J. Geophys. Res. **98**, 14109 (1993).

[13] A. Crisanti, M. H. Jensen, A. Vulpiani, and G. Paladin, Strongly intermittent chaos and scaling in an earthquake model, Phys. Rev. A **46**, R7363(R) (1992).

[14] R. Burridge and L. Knopoff, Model and theoretical seismicity, Bull. Seismol. Soc. Am. **57**, 341 (1967).

[15] B. Gutenberg and C. F. Richter, Earthquake magnitude, intensity, energy, and acceleration, Bull. Seismol. Soc. Am. **46**, 105 (1956)

[16] B. Gutenberg and C. F. Richter, Frequency of earthquakes in California, Bull. Seismol. Soc. Am. **34**, 185 (1944).

[17] F. F. Csikor, C. Motz, D. Weygand, M. Zaiser, and S. Zapperi, Dislocation avalanches, strain bursts, and the problem of plastic forming at the micrometer scale, Science **318**, 251 (2007).

[18] S. Poincloux, M. Adda-Bedia, and F. Lechenault, Crackling Dynamics in the Mechanical Response of Knitted Fabrics, Phys. Rev. Lett. **121**, 058002 (2018).

[19] B. Alessandro, C. Beatrice, G. Bertotti, and A. Montorsi, Domain-wall dynamics and Barkhausen effect in metallic ferromagnetic materials. I. Theory, J. Appl. Phys. **68**, 2901 (1990).

[20] B. Alessandro, C. Beatrice, G. Bertotti, and A. Montorsi, Domain-wall dynamics and Barkhausen effect in metallic ferromagnetic materials. II. Experiments, J. Appl. Phys. **68**, 2908 (1990).

[21] R. Vergne, J. C. Cotillard, and J. L. Porteseil, Quelques aspects statistiques des processus d'aimantation dans les corps ferromagnétiques. Cas du déplacement d'une seule paroi de Bloch à 180° dans un milieu monocristallin aléatoirement perturbé, Rev. Phys. Appl. (Paris) **16**, 449 (1981).

[22] P. Le Doussal, K. J. Wiese, and P. Chauve, Functional renormalization group and the field theory of disordered elastic systems, Phys. Rev. E **69**, 026112 (2004).

[23] P. Le Doussal, K. J. Wiese, and P. Chauve, Two-loop functional renormalization group analysis of the depinning transition, Phys. Rev. B **66**, 174201 (2002).

[24] P. Chauve, P. Le Doussal, and K. J. Wiese, Renormalization of Pinned Elastic Systems: How Does It Work Beyond One Loop? Phys. Rev. Lett. **86**, 1785 (2001).

[25] A. A. Fedorenko and S. Stepanow, Depinning transition at the upper critical dimension, Phys. Rev. E **67**, 057104 (2003).

[26] P. Le Doussal and K. J. Wiese, Higher correlations, universal distributions and finite size scaling in the field theory of depinning, Phys. Rev. E **68**, 046118 (2003).

[27] K. J. Wiese and P. Le Doussal, Functional renormalization for disordered systems: Basic recipes and gourmet dishes, Markov Processes Relat. Fields **13**, 777 (2007).

[28] K. J. Wiese, Theory and experiments for disordered elastic manifolds, depinning, avalanches, and sandpiles, arXiv:2102.01215.

[29] A. A. Middleton, P. Le Doussal, and K. J. Wiese, Measuring Functional Renormalization Group Fixed-Point Functions for Pinned Manifolds, Phys. Rev. Lett. **98**, 155701 (2007).

[30] A. Rosso, P. Le Doussal, and K. J. Wiese, Numerical calculation of the functional renormalization group fixed-point functions at the depinning transition, Phys. Rev. B **75**, 220201(R) (2007).

[31] P. Le Doussal and K. J. Wiese, Avalanche dynamics of elastic interfaces, Phys. Rev. E **88**, 022106 (2013).

[32] Z. Zhu and K. J. Wiese, The spatial shape of avalanches, Phys. Rev. E **96**, 062116 (2017).
[33] P. Le Doussal and K. J. Wiese, Driven particle in a random landscape: disorder correlator, avalanche distribution and extreme value statistics of records, Phys. Rev. E **79**, 051105 (2009).
[34] S. Bustingorry, A. B. Kolton, and T. Giamarchi, Random-manifold to random-periodic depinning of an elastic interface, Phys. Rev. B **82**, 094202 (2010).
[35] P. Le Doussal and K. J. Wiese, How to measure Functional RG fixed-point functions for dynamics and at depinning, Europhys. Lett. **77**, 66001 (2007).
[36] W. Wasow, *Asymptotic Expansions for Ordinary Differential Equations*, Pure and Applied Mathematics, Vol. XIV (Interscience, New York, 1965).
[37] N. N. Bogolyubov, Jr., Perturbation theory, in *Encyclopedia of Mathematics* (2011), https://encyclopediaofmath.org/wiki/Perturbation_theory.
[38] D. R. Smith, *Singular-Perturbation Theory* (Cambridge University Press, Cambridge, 1985).
[39] E. Hairer and G. Wanner, *Solving Ordinary Differential Equations II: Stiff and Differential-Algebra Problems* (Springer, Berlin, 1996).
[40] G. Bertotti, *Hysteresis and Magnetism* (Academic, San Diego, 1998).
[41] F. Colaiori, Exactly solvable model of avalanches dynamics for Barkhausen crackling noise, Adv. Phys. **57**, 287 (2008).
[42] A. Dobrinevski, P. Le Doussal, and K. J. Wiese, Non-stationary dynamics of the Alessandro-Beatrice-Bertotti-Montorsi model, Phys. Rev. E **85**, 031105 (2012).
[43] C. ter Burg, Ph.D. thesis, PSL Research University, 2021.
[44] P. Mörters and Y. Peres, *Brownian Motion*, Cambridge Series in Statistical and Probabilistic Mathematics (Cambridge University Press, Cambridge, 2010).
[45] L. Benigni, C. Cosco, A. Shapira, and K. J. Wiese, Hausdorff dimension of the record set of a fractional Brownian motion, Electron. Commun. Probab. **23**, 1 (2018).
[46] A. A. Middleton, Asymptotic Uniqueness of the Sliding State for Charge-Density Waves, Phys. Rev. Lett. **68**, 670 (1992).
[47] I. Dornic, H. Chaté, and M. A. Muñoz, Integration of Langevin Equations with Multiplicative Noise and the Viability of Field Theories for Absorbing Phase Transitions, Phys. Rev. Lett. **94**, 100601 (2005).
[48] A. Dobrinevski, Field theory of disordered systems–Avalanches of an elastic interface in a random medium, Ph.D. thesis, ENS Paris, 2013.
[49] A. Kolton, P. Le Doussal, and K. J. Wiese, Distribution of velocities in an avalanche, and related quantities: Theory and numerical verification, Europhys. Lett. **127**, 46001 (2019).
[50] M. A. Muñoz, Multiplicative noise in non-equilibrium phase transitions: A tutorial, in *Advances in Condensed Matter and Statistical Physics*, edited by E. Korutcheva and R. Cuerno (Nova Science, Hauppauge, NY, 2004), pp. 37–68.